Conference Note

tag: sPH-CONF-JET-2026-01
date: June 19, 2026

sPHENIX Conference Note

Precise measurement of jet energy scale derived from *in situ* techniques using γ-jet and multijet transverse momentum balance in p+p collisions at $\sqrt{s}$=200 GeV with the sPHENIX detector

sPHENIX Collaboration

Abstract

The response of the sPHENIX calorimeter system to jets is calibrated using *in situ* techniques in p+p collisions at $\sqrt{s}$ = 200 GeV provided by the Relativistic Heavy Ion Collider. Events in which a jet recoils against a reference object with an independently-determined energy scale are studied, comprising photon-jet and multijet processes. The response in data is compared to that in Monte Carlo simulation. Data-to-Monte Carlo jet energy scale ratios are examined and final corrections are derived as a function of jet transverse momentum and jet radius parameter. The corrections are 1–2% with uncertainties ranging from 3–4% over the jet transverse momentum range 10–60 GeV. These constraints are critical for the precision sPHENIX jet physics program in p+p and heavy-ion collisions.

1 Introduction

The sPHENIX experiment at the Relativistic Heavy Ion Collider (RHIC) [1] was designed to carry out a state-of-the-art reconstructed jet physics program in high-energy nuclear collisions. Measurements of jet cross sections, dijet correlations, and jet (sub-)structure utilizing the sPHENIX calorimeters require a detailed understanding of the jet energy scale (JES) in the detector. After simulation-derived calibrations account for the average response, pileup, and absolute energy scale effects, *in situ* methods are used to compare observables sensitive to the jet response in p+p data and Monte Carlo (MC) simulation. These comparisons are based on the expected transverse momentum (p_{T}) balance between jets and objects with independently-determined energy scales and are performed in well-understood physics processes. They provide an independent data driven validation of the JES and can be used to derive small calibration factors which account for residual mis-modeling in the simulations and thus equalize the response to that observed in data.

In situ methods have been used in experiments at the Tevatron [2, 3] and the Large Hadron Collider [4, 5, 6] to derive this final calibration step or verify the full jet calibration sequence. At the LHC, the primary *in situ* methods rely on momentum balance in γ-jet and Z-jet events, where the photon or dilepton system provides a high-precision reference. In these topologies, the jet response is extracted from the ratio $x_J = p_{\mathrm{T}}^{\mathrm{jet}}/p_T^{\mathrm{ref}}$ after correcting for additional radiation and resolution effects. Multijet balance techniques, in which a jet is kinematically balanced by multiple lower-p_{T} jets, can be used to extend the calibration to higher transverse momentum where the γ/Z-jet statistics are limited. These complementary channels ensure broad coverage across the jet p_{T} range and in different regions of the detector. The resulting *in situ* Data-to-MC JES corrections are propagated to jet physics measurements, where they often constitute a leading systematic uncertainty in precision measurements and searches for new phenomena. Continuous validation with data over the running period is therefore essential to maintaining percent-level control of jet-related uncertainties.

This note concerns measurements of the Data-to-MC JES correction performed with the sPHENIX calorimeter system [7] in p+p collision data at $\sqrt{s} = 200$ GeV recorded during RHIC Run-24 in June–October 2024. The analysis is performed for anti-k_t [8] jets with radius parameter ranging from $R = 0.2$–0.8. For the sPHENIX experiment, the primary *in situ* channel is balanced γ-jet events, which constrains the JES over jet $p_{\mathrm{T}} \approx 10$–$30$ GeV. Multijet events using $R = 0.4$ jets are used to extend the Data-to-MC JES correction from the region constrained by γ-jet data to higher jet p_{T} values up to 60 GeV.

A global fit incorporating both γ-jet and multijet observables is performed to determine calibration factors which result in the optimal agreement between data and simulation. The associated systematic uncertainties are also evaluated. The global fit results for $R = 0.4$ jets are then transferred to the other jet R values. In this method, the Data-to-MC JES correction is evaluated statistically over an ensemble of jets, and not from the individual properties of each jet.

2 Data and simulation samples

A detailed description of the sPHENIX detector is available in Ref. [9]. The measurements presented here use the Minimum Bias Detector (MBD), the electromagnetic (EMCal) and hadronic

(HCal) calorimeter system, and the Level-1 trigger system. The compact EMCal is based on a tungsten-scintillator sampling design, with fine spatial and energy resolution for photon and electron measurements, and is calibrated tower-by-tower using the π^0 and $\eta \rightarrow \gamma\gamma$ invariant mass. The electromagnetic energy scale is well determined with a systematic uncertainty of 1.5% depending on photon energy [10]. For full jet reconstruction and triggering, the HCal comprises inner and outer sections located inside and outside the solenoid magnet and is designed with scintillating tiles sandwiched between titled absorber plates. The HCal is calibrated using cosmic-ray muons and temperature-dependent corrections. The full calorimeter system provides approximately five nuclear interaction lengths, complete coverage in azimuth, and wide pseudorapidity acceptance for jets produced at RHIC kinematics ($|\eta| < 1.1$).

Event characterization and timing are provided by the Minimum Bias Detector (MBD), which consists of fast Cherenkov detectors located at forward and backward rapidities ($3.51 < |\eta| < 4.61$), enabling precise determination of the collision time, vertex position, and, in large collision systems, event centrality. In the Level-1 hardware trigger system, photon triggers were defined using the sum of EMCal energies within fixed windows with various programmable thresholds. Calorimeter-based jet triggers were defined using the sum of EMCal and HCal energies within sliding windows of approximately $\Delta\eta \times \Delta\phi = 0.8 \times 0.8$, also with varying thresholds.

The 2024 dataset comprises two p+p running periods: a primary period with zero beam crossing angle and collision z-vertex distribution width of 55–60 cm, and a secondary period with a 1.5 mrad crossing angle and narrower vertex distributions of 15–20 cm. Events were required to have an MBD-reconstructed z-vertex within $|z_{\text{MBD}}| < 60$ cm and a collision time within $|t_{\text{MBD}}| < 20$ ns centered on the mean beam crossing time to reduce non-collision background. For the γ-jet analysis, events were selected by requiring a Level-1 photon trigger with a 5 GeV threshold in coincidence with the minimum-bias trigger, defined by requiring at least one MBD tube above threshold on each side. The photon trigger is fully efficient for the entire γ-jet photon p_{T} range utilized here. For the multijet analysis, events were selected using a coincidence of the jet trigger with a 10 GeV threshold and the minimum-bias trigger.

Two MC event generators are used for comparisons to γ-jet and multijet events in data. Pythia-8, version 8.312 [11], was used with the Detroit tune, optimized for jet observables at RHIC energies [12]. Multiple thresholds on the minimum parton-level scattering p_{T} were combined to populate the physically falling p_{T} distributions for the γ-jet or multijet samples. The γ-jet samples include direct photons and also fragmentation photons from $2 \rightarrow 2$ QCD processes, with the relative weighting as given by Pythia-8. Additionally the MC generator Herwig-7.3 [13, 14] was used with the Nashville tune [15].

MC events were propagated through the full sPHENIX detector simulation using Geant-4 [16], including emulation of calorimeter noise at levels determined from 2024 p+p data, and then reconstructed and calibrated identically to data. Jets using these fully simulated calorimeter tower energies are referred to as reconstructed-level jets. In the generators, particle-level jets are defined by applying the anti-k_t algorithm directly to all truth final-state particles, excluding muons and neutrinos.

3 Jet and photon reconstruction

Jets and photons are reconstructed using the sPHENIX calorimeter system. A detailed description of the calorimeter jet reconstruction in p+p collisions is given in Ref. [17] and is summarized here. Jets are reconstructed by applying the anti-k_t algorithm [8, 18] to EMCal and HCal towers, with the finer EMCal towers grouped together into "pseudo-towers" to match the larger $\Delta\eta$ and $\Delta\phi$ segmentation of the HCal towers. Jet radius parameters ranging from $R = 0.2$–0.8 are used. Jets are calibrated for the average detector response using an initial JES correction derived from the Pythia-8 simulation samples. For the calibration method considered here, this initial correction depends on the R parameter, the measured jet p_{T}, jet η, and the event z_{MBD}. In the simulation, the jet energy is smeared by an additional factor (and thus the jet energy resolution (JER) is increased) which is derived from data-driven studies of the *in situ* dijet balance [17]. The data-driven JER studies were not performed for $R = 0.2$ jets, due to the weaker detector- and physics-level p_{T} correlations for dijets of this radius. Thus given that the JER smearing was nearly jet radius independent, the $R = 0.3$ smearing is utilized for $R = 0.2$ as well.

A detailed description of the photon reconstruction and selection in p+p collisions is given in Ref. [10] and is summarized here. EMCal clusters are reconstructed from contiguous groupings of EMCal towers with a measured energy significantly above the local pedestal noise level, and then split along local maxima using an algorithm similar to that in Ref. [19]. EMCal clusters which likely originate from the showering of single photons, rather than boosted neutral meson decays or the start of hadron showers, are identified on the basis of their shower shape. This likelihood is quantified using a Boosted Decision Tree (BDT) trained on five variables that quantify aspects of the shower shape, such as the energy-weighted width of the cluster in η or the ratio of the maximal-energy tower relative to its neighbors. BDT scores range from 0 (background-like) to 1 (signal-like). EMCal clusters are further classified by their isolation energy, defined as the sum of the transverse energy in the full calorimeter system within a 0.4 cone centered on the cluster, excluding the contribution from the cluster itself.

Figure 1 shows the distribution of EMCal cluster BDT scores and isolation energies in data (which includes background contributions) and Pythia-8 γ-jet simulation. In this analysis, signal photons in data are defined as those with a BDT score > 0.9 and an isolation energy < 2 GeV. The identical selections are also applied in simulation. This requirement is tighter than that used in the measurements of the isolated photon cross-section [10] to ensure a high purity of photons in the selected sample. In this analysis, the residual impurity is not explicitly corrected for and the potential impact is evaluated by considering alternative identification and isolation requirements.

For both reconstructed jets and photons in data, additional requirements, based on the arrival time measured in the calorimeter with respect to the collision, were applied to remove non-collision backgrounds. These backgrounds include beam-gas collisions, uncollimated beam particles, and cosmic rays.

4 *In situ* γ-jet analysis

First, the *in situ* constraint is calculated using only the γ-jet results, and in Section 6 is combined with the multijet results for a global constraint. The γ-jet analysis is performed at the reconstructed

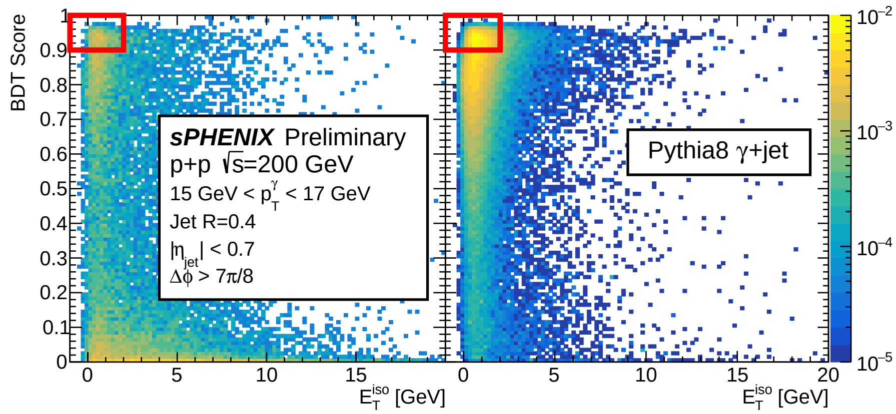

Figure 1: Distribution of isolation energies and BDT scores of EMCal clusters with $p_{\mathrm{T}}^{\gamma} = 15$–$17$ GeV in p+p (left) collision data and (right) Pythia-8 γ-jet simulations. The band in the bottom left that exists in data but not in simulation is made of decay photons which are rejected by the BDT cut. Here, only clusters with an away-side jet, as described in Section 4, are plotted. The selected signal region is shown in the red box.

level for the photon-triggered events in data and the γ-jet samples in simulation. Events are analyzed where the leading (highest-p_{T}) photon passes identification and isolation selections and has $p_{\mathrm{T}}^{\gamma} > 10$ GeV. The leading jet, among those which have $p_{\mathrm{T}}^{\mathrm{jet}} > 5$ GeV and are not within $\Delta R = \sqrt{\Delta\eta^2 + \Delta\phi^2} < R$ of the photon, are then selected. The photon and jet are required to be within $|\eta^{\gamma}| < 1.1$ and $|\eta^{\mathrm{jet}}| < 1.1 - R$ to ensure full containment of the jet area in the calorimeter. The pair is also required to satisfy $\Delta\phi = |\phi^{\gamma} - \phi^{\mathrm{jet}}| > 7\pi/8$.

The jet-to-photon p_{T} ratio ($x_{J\gamma} = p_{\mathrm{T}}^{\mathrm{jet}} \,/\, p_{\mathrm{T}}^{\gamma}$) is calculated in different p_{T}^{γ} intervals. Figure 2 shows a comparison of the $x_{J\gamma}$ distributions for $R = 0.4$ jets in data and Pythia-8 simulation. At lower p_{T}^{γ}, the distributions have a sharp cutoff at a particular value of $x_{J\gamma}$, which results from the minimum $p_{\mathrm{T}}^{\mathrm{jet}}$ threshold with respect to the p_{T}^{γ} range. The $x_{J\gamma}$ distributions are analyzed only in bins strictly above this cutoff. At higher p_{T}^{γ}, the $x_{J\gamma}$ distributions feature a pronounced peak, reflecting the approximate p_{T} balance of the γ-jet topology. Figure 2 also shows the arithmetic mean of the distributions ($\langle x_{J\gamma} \rangle$). Table 1 summarizes the extracted mean values in data, simulation, and their ratios.

Figure 3 compares the $\langle x_{J\gamma} \rangle$ as a function of p_{T}^{γ} in data and Pythia-8 simulation. The γ-jet data allow for a constraint on the Data-to-MC JES over the p_{T} range 10–30 GeV. Corrections to the jet p_{T} may potentially take any form dependent on p_{T}. However, given the limited p_{T} range and statistics of the γ-jet sample, the correction is assumed to be p_{T}-independent, i.e., $C(p_{\mathrm{T}}) = a$. Parameter values are scanned and the global minimum where the smallest total χ^2 between data and simulation, χ^2_{best}, is determined. The statistical uncertainty on the parameter is defined by the parameter region where $\chi^2 < \chi^2_{\mathrm{best}} + 1$. The potential p_{T} dependence of the correction is evaluated using multijet balance techniques in Section 6, where the correction function takes the form $C(p_{\mathrm{T}}) = a + b p_{\mathrm{T}}$.

The lowest three p_{T} intervals have reduced sensitivity to the Data-to-MC JES correction because

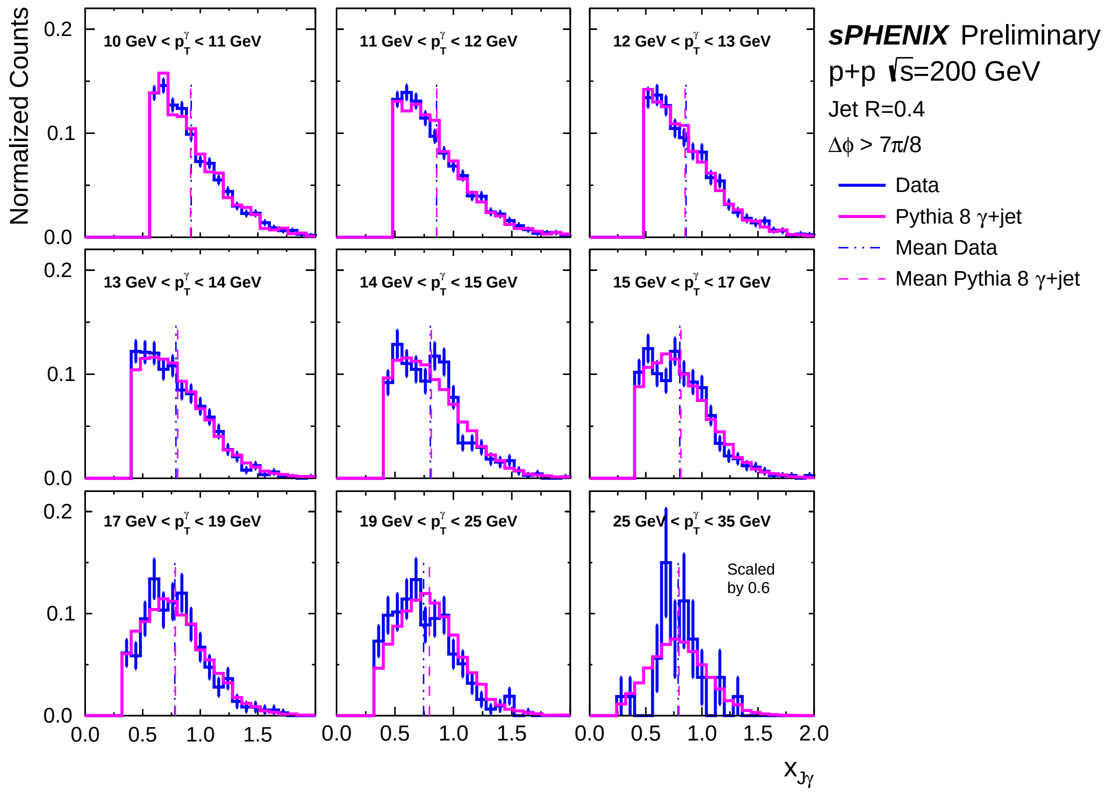

Figure 2: Distributions of $x_{J\gamma}$ for $R = 0.4$ jets, shown separately for each p_{T}^{γ}interval in p+p data and reconstructed-level PYTHIA-8 simulation. Statistical uncertainties on the data are shown as error bars, meanwhile the statistical uncertainties on the simulation are significantly smaller and not shown. The dashed and dash-dotted lines indicate the mean $x_{J\gamma}$ values.

the kinematic region explored does not produce a well-defined peak in the $x_{J\gamma}$ distribution. Additionally, the highest two p_{T} intervals have limited sensitivity due to their large statistical uncertainties. To evaluate the impact of these intervals, the global fit was repeated under two unique conditions: once excluding the lowest three p_{T} intervals and once excluding the highest two p_{T} intervals. The resulting fit parameter does not change within uncertainties. Therefore, all p_{T} intervals from the γ-jet analysis were retained.

p_T^γ Range	$\langle x_{J\gamma}\rangle$ (Data)	$\langle x_{J\gamma}\rangle$ (PYTHIA-8)	$\langle x_{J\gamma}\rangle_{\text{Data}} / \langle x_{J\gamma}\rangle_{\text{PYTHIA-8}}$
10-11 GeV	0.921 ± 0.005 GeV	0.916 ± 0.006 GeV	1.006 ± 0.008
11-12 GeV	0.856 ± 0.005 GeV	0.858 ± 0.006 GeV	0.998 ± 0.009
12-13 GeV	0.859 ± 0.007 GeV	0.850 ± 0.005 GeV	1.010 ± 0.010
13-14 GeV	0.788 ± 0.008 GeV	0.804 ± 0.002 GeV	0.981 ± 0.011
14-15 GeV	0.802 ± 0.010 GeV	0.811 ± 0.003 GeV	0.990 ± 0.013
15-17 GeV	0.803 ± 0.010 GeV	0.813 ± 0.002 GeV	0.988 ± 0.013
17-19 GeV	0.779 ± 0.014 GeV	0.784 ± 0.003 GeV	0.994 ± 0.019
19-25 GeV	0.745 ± 0.015 GeV	0.794 ± 0.003 GeV	0.938 ± 0.019
25-35 GeV	0.788 ± 0.038 GeV	0.796 ± 0.002 GeV	0.991 ± 0.048

Table 1: Summary of $\langle x_{J\gamma}\rangle$ values and their ratios between data and PYTHIA-8 simulation for different p_T^γ intervals for $R = 0.4$ jets. The uncertainties quoted are statistical only.

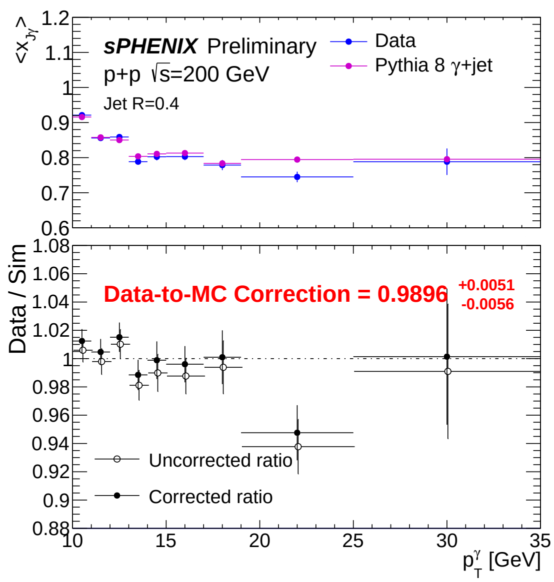

Figure 3: The top panel shows the $\langle x_{J\gamma}\rangle$ as a function of p_T^γ for $R = 0.4$ jets in data and PYTHIA-8 simulation. The bottom panel shows the ratio of $\langle x_{J\gamma}\rangle$ between data and simulation before and after Data-to-MC JES correction. A dashed line is drawn at 1 for a reference, and the points are slightly offset for visual clarity. The correction parameter a and the associated statistical uncertainty are quoted.

4.1 Systematic uncertainties

The sensitivity of the extracted Data-to-MC JES correction to the following systematic effects is investigated: (i) the purity of the selected photon sample in data, (ii) the γ-jet event topology selection, (iii) the modeling of the JER, (iv) the electromagnetic scale of the EMCal, and (v) the physics model dependence. In each case, the data and/or simulation was re-analyzed under different conditions, and the difference in the results to the nominal was considered as a systematic uncertainty. For the sources where only one variation was performed, the uncertainty is taken to be symmetric with the magnitude in each direction given by this single variation. The systematic uncertainties from all sources were added in quadrature to determine the total uncertainty.

(i) Controlling the purity of the selected photons in data is a critical aspect of the analysis as backgrounds from, e.g., $\pi^0 \rightarrow \gamma\gamma$, will have a different associated-jet p_{T} distribution. The selection based on BDT score and isolation energy is designed to provide a high-purity sample but will nevertheless contain an admixture of background. To evaluate the impact of this uncertainty, the BDT score and isolation energy requirements are separately loosened and tightened to > 0.7 and to < 1.5 GeV, respectively, which modify the purity of the photon sample in data.

(ii) While in a leading-order picture the photon and jet are produced approximately back to back, radiation at large angles outside the jet cone is expected to contribute to the shape of the $x_{J\gamma}$ distribution. The event topology selection uncertainty tests the sensitivity of the results to this aspect of the modeling in simulation. This uncertainty is evaluated by rejecting events, in both data and simulation, where an additional jet with $p_{\mathrm{T}} > 5$ GeV is present anywhere in the sPHENIX acceptance. This variation raises the $\langle x_{J\gamma} \rangle$ in data and simulation by a p_{T}-dependent factor, but by a similar amount such that the effect in the $\langle x_{J\gamma} \rangle$ ratio is small, reflecting the good modeling of these topologies in simulation.

(iii) There is a Data-to-MC determined additional JER smearing. To evaluate the sensitivity of these results to this effect, the additional JER smearing is varied by $\approx \pm 2\%$, as documented in Ref. [17].

(iv) The electromagnetic scale has an uncertainty of $\pm 1.5\%$ as constrained by the π^0 and η mass studies. The electromagnetic calorimeter response is varied up and down for both the photon and the portion of the jet energy measured in the EMCal. Thus, the resulting variation in the $x_{J\gamma}$is smaller than $\pm 1.5\%$.

(v) The data-simulation comparisons discussed above have been evaluated using Pythia-8. To test the sensitivity of the results to the physics modeling, the data is compared to Herwig-7.3, which has a significantly different treatment of parton showering and hadronization. Figure 4 shows a comparison of the γ-jet $x_{J\gamma}$ distributions between data and Herwig-7.3 simulation. The values and ratios for $\langle x_{J\gamma} \rangle$ are shown in Table 2. Figure 5 shows the fit results and the extracted Data-to-MC JES correction parameter a. For this systematic variation, the Pythia-8 simulation acts as the nominal correction while the uncertainty is determined by the difference between default and Herwig-7.3.

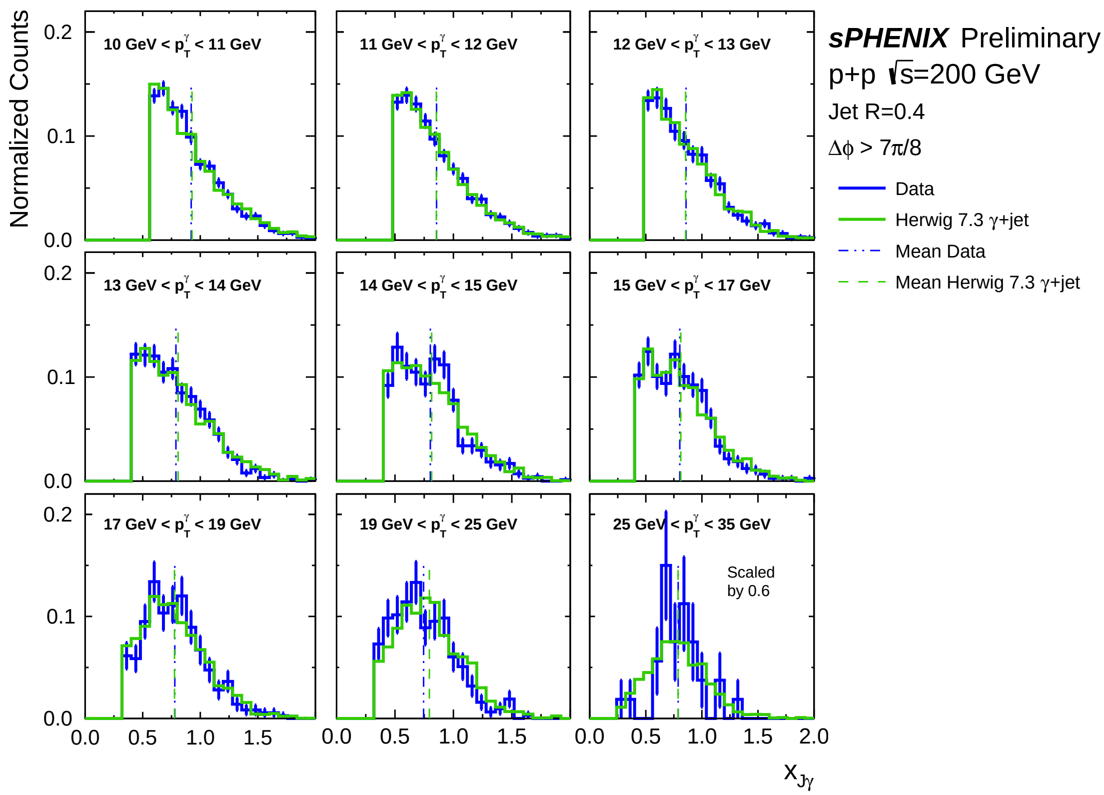

Figure 4: Distributions of $x_{J\gamma}$ for $R = 0.4$ jets, shown separately for each p_T^γ interval in p+p data and reconstructed-level HERWIG-7.3 simulation. Statistical uncertainties on the data are shown as error bars, meanwhile the statistical uncertainties on the simulation are significantly smaller and not shown. The dashed and dash-dotted lines indicate the mean $x_{J\gamma}$ values.

p_T^γ Range	$\langle x_{J\gamma}\rangle$ (Data)	$\langle x_{J\gamma}\rangle$ (HERWIG-7.3)	$\langle x_{J\gamma}\rangle_{\text{Data}}/\langle x_{J\gamma}\rangle_{\text{HERWIG-7.3}}$
10-11 GeV	0.921 ± 0.005 GeV	0.928 ± 0.005 GeV	0.992 ± 0.007
11-12 GeV	0.856 ± 0.005 GeV	0.854 ± 0.004 GeV	1.002 ± 0.008
12-13 GeV	0.859 ± 0.007 GeV	0.855 ± 0.006 GeV	1.005 ± 0.011
13-14 GeV	0.788 ± 0.008 GeV	0.807 ± 0.006 GeV	0.976 ± 0.013
14-15 GeV	0.802 ± 0.010 GeV	0.814 ± 0.008 GeV	0.986 ± 0.016
15-17 GeV	0.803 ± 0.010 GeV	0.812 ± 0.007 GeV	0.989 ± 0.015
17-19 GeV	0.779 ± 0.014 GeV	0.776 ± 0.009 GeV	1.004 ± 0.022
19-25 GeV	0.745 ± 0.015 GeV	0.794 ± 0.007 GeV	0.938 ± 0.020
25-35 GeV	0.788 ± 0.038 GeV	0.788 ± 0.008 GeV	1.001 ± 0.049

Table 2: Summary of $\langle x_{J\gamma}\rangle$ values and their ratios between data and HERWIG-7.3 for different p_T^γintervals with $R = 0.4$ jets. The uncertainties quoted are statistical only.

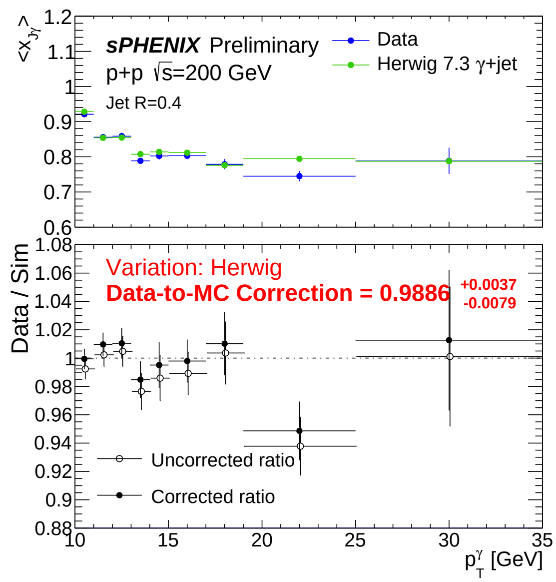

Figure 5: The top panel shows the $\langle x_{J\gamma} \rangle$ as a function of p_T^γ for $R = 0.4$ jets in data and Herwig-7.3 simulation. The bottom panel shows the ratio of $\langle x_{J\gamma} \rangle$ between data and simulation before and after Data-to-MC JES correction. A dashed line is drawn at 1 for a reference, and the points are slightly offset for visual clarity. The correction parameter a and the associated statistical uncertainty are quoted.

4.2 Data-to-MC JES correction from γ-jet

The γ-jet analysis procedure was repeated for all jet R values. In all cases, the resulting Data-to-MC JES corrections are independent of jet p_{T} within uncertainties. Table 3 summarizes these corrections and their statistical and systematic uncertainties. For $R = 0.4$ jets, the total uncertainty is dominated by the photon purity, including both BDT and isolation variations. Meanwhile, the physics modeling uncertainty dominates for other jet R values. The correction factors for all the examined R values are consistent within uncertainties.

Jet Radius	Data-to-MC JES Correction	BDT	Isolation	Jet Topology	Model	JER	EM Scale
0.2	$0.9957^{+0.0043}_{-0.0093}$ (stat) $^{+0.0333}_{-0.0335}$ (sys)	0.0165	0.0166	0.0045	0.0233	$^{+0.0000}_{-0.0037}$	$^{+0.0043}_{-0.0000}$
0.3	$1.0000^{+0.0029}_{-0.0074}$ (stat) $^{+0.0320}_{-0.0327}$ (sys)	0.0161	0.0090	0.0060	0.0254	$^{+0.0007}_{-0.0069}$	$^{+0.0009}_{-0.0007}$
0.4	$0.9896^{+0.0051}_{-0.0056}$ (stat) $^{+0.0247}_{-0.0252}$ (sys)	0.0229	0.0087	0.0029	0.0010	$^{+0.0010}_{-0.0046}$	$^{+0.0004}_{-0.0014}$
0.5	$0.9862^{+0.0026}_{-0.0058}$ (stat) $^{+0.0287}_{-0.0287}$ (sys)	0.0210	0.0135	0.0032	0.0139	$^{+0.0000}_{-0.0000}$	$^{+0.0000}_{-0.0000}$
0.6	$0.9863^{+0.0069}_{-0.0016}$ (stat) $^{+0.0406}_{-0.0403}$ (sys)	0.0199	0.0112	0.0056	0.0327	$^{+0.0049}_{-0.0000}$	$^{+0.0000}_{-0.0056}$
0.7	$0.9850^{+0.0020}_{-0.0019}$ (stat) $^{+0.0497}_{-0.0497}$ (sys)	0.0232	0.0060	0.0114	0.0420	$^{+0.0002}_{-0.0000}$	$^{+0.0000}_{-0.0002}$
0.8	$0.9867^{+0.0107}_{-0.0038}$ (stat) $^{+0.0573}_{-0.0573}$ (sys)	0.0187	0.0047	0.0167	0.0513	$^{+0.0000}_{-0.0000}$	$^{+0.0004}_{-0.0056}$

Table 3: Table of Data-to-MC JES correction results and uncertainties for different anti-k$_t$ jet radius parameters from the γ-jet constraint alone.

5 Multijet balancing method

The multijet balancing method (MBM) is used to extend the Data-to-MC JES correction to jets beyond the p_T range directly accessible with the γ-jet calibration. In this method, events are selected with one high-p_T leading jet balanced by two lower-p_T jets on the opposite side in azimuth. The p_T of the leading, and two sub-leading jets are denoted as $p_{\mathrm{T},1}$, $p_{\mathrm{T},2}$, and $p_{\mathrm{T},3}$, respectively. This configuration allows the JES calibration, which is well constrained by the γ-jet measurements for the p_T of the two sub-leading jets, to be extended to higher jet p_T. This approach follows the general procedure established by the ATLAS experiment [6]. The MBM analysis provides constraints up to a jet p_T of 60 GeV. To ensure that the sub-leading and tertiary jets are within the p_T region where the JES is well constrained by the γ-jet calibration, they are required to satisfy $7\,\mathrm{GeV} \leq p_{\mathrm{T},2}, p_{\mathrm{T},3} \leq 30$ GeV. Furthermore, to ensure good statistical power in the data, the MBM analysis is performed using $R = 0.4$ jets and the results are extended to other R values in the procedure described below.

Events are required to have a leading jet with $p_{\mathrm{T},1} > 20$ GeV and at least two other jets with $p_{\mathrm{T},2}, p_{\mathrm{T},3} > 7$ GeV, where the leading and subleading jets are separated by $\Delta\phi_{1,2} \geq 3\pi/4$ in azimuth and the leading and tertiary jets are separated by $\Delta\phi_{1,3} \geq \pi/2$, i.e., the two lower-$p_\mathrm{T}$ jets are in the same hemisphere opposite the leading jet. All selected jets are required to be contained within the calorimeter acceptance, $|\eta^{\mathrm{jet}}| < 1.1 - R$, where in this case $R = 0.4$. After satisfying these requirements, we define a recoil jet with $p_{\mathrm{T},2+3}$, the vector-sum of $\vec{p}_{\mathrm{T},2}$ and $\vec{p}_{\mathrm{T},3}$.

To quantify the transverse momentum balance between the leading jet and the recoil jet, the multijet x_J is defined by $x_J = p_{T,2+3}/p_{T,1}$. However, to conceptually match the intention of the $x_{J\gamma}$ quantity, in which the better-known reference p_T is in the denominator, we report instead the inverse quantity $x_J^{-1} = p_{T,1}/p_{T,2+3}$, since in the MBM analysis the two lower-p_T jets are the "reference", as constrained by the *in situ* γ-jet analysis.

Figure 6 shows multijet x_J distributions from data and Pythia-8 simulation for different $p_{\mathrm{T},1}$ intervals. The data and Pythia-8 distributions have qualitatively similar shapes, with a peak corresponding to approximately balanced multijet systems. The mean value, $\langle x_J^{-1}\rangle$, is determined from the arithmetic mean over the entire distribution. The mean values in data and simulation and their ratios are shown in Table 4. The ratios are generally consistent with unity within statistical uncertainties.

$p_{T,1}$ Range	$\langle x_J^{-1}\rangle$ (Data)	$\langle x_J^{-1}\rangle$ (Pythia-8)	$\langle x_J{}^{-1}\rangle_{\mathrm{Data}}/\langle x_J{}^{-1}\rangle_{\mathrm{Pythia\text{-}8}}$
20-25 GeV	1.141 ± 0.002	1.130 ± 0.003	1.009 ± 0.004
25-30 GeV	1.253 ± 0.005	1.250 ± 0.004	1.003 ± 0.007
30-35 GeV	1.348 ± 0.010	1.346 ± 0.005	1.001 ± 0.011
35-40 GeV	1.445 ± 0.020	1.431 ± 0.006	1.010 ± 0.021
40-50 GeV	1.516 ± 0.036	1.517 ± 0.007	0.999 ± 0.036
50-60 GeV	1.642 ± 0.112	1.689 ± 0.014	0.972 ± 0.113

Table 4: Multijet x_J^{-1} results in data and Pythia-8 simulation and their ratio for $R = 0.4$ jets. Only statistical uncertainties are shown.

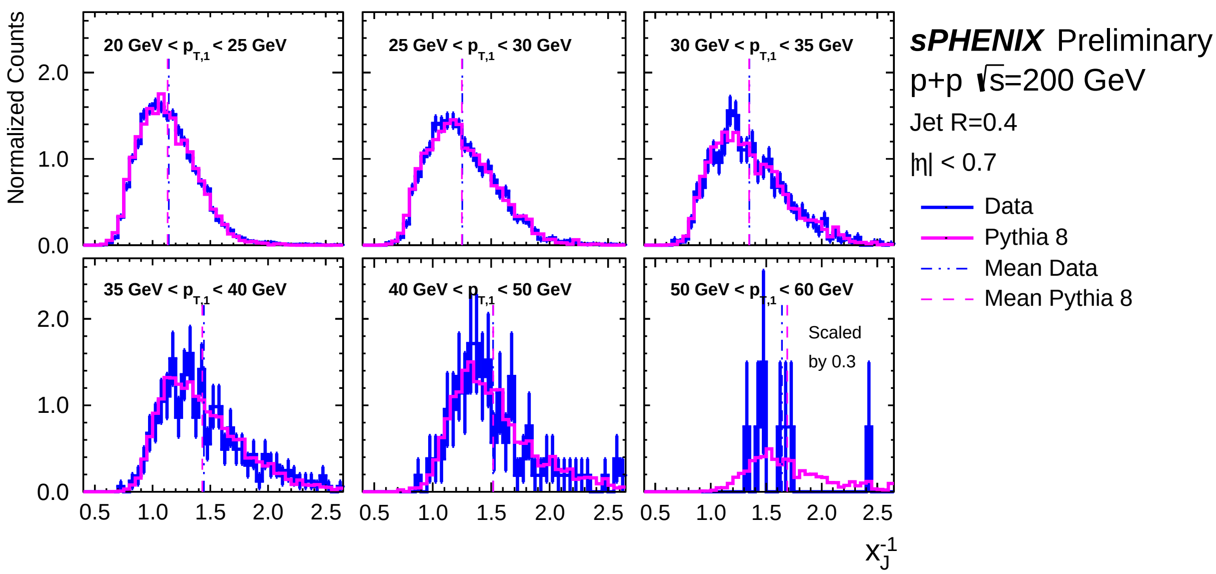

Figure 6: Distributions of multijet x_J^{-1} for the MBM analysis of $R = 0.4$ jets, shown for each $p_{\mathrm{T},1}$ interval in p+p data and reconstructed-level Pythia-8 simulation. Statistical uncertainties on the data are shown as error bars, meanwhile the statistical uncertainties on the simulation are significantly smaller and not shown.

For the MBM analysis, two systematic uncertainties were investigated, which are analogous to those in the γ-jet analysis above: (i) the modeling of the JER in simulation, and (ii) the physics model dependence. For the latter, Figure 7 and Table 5 summarize the comparison of the MBM results in data to that in the HERWIG-7.3 simulation.

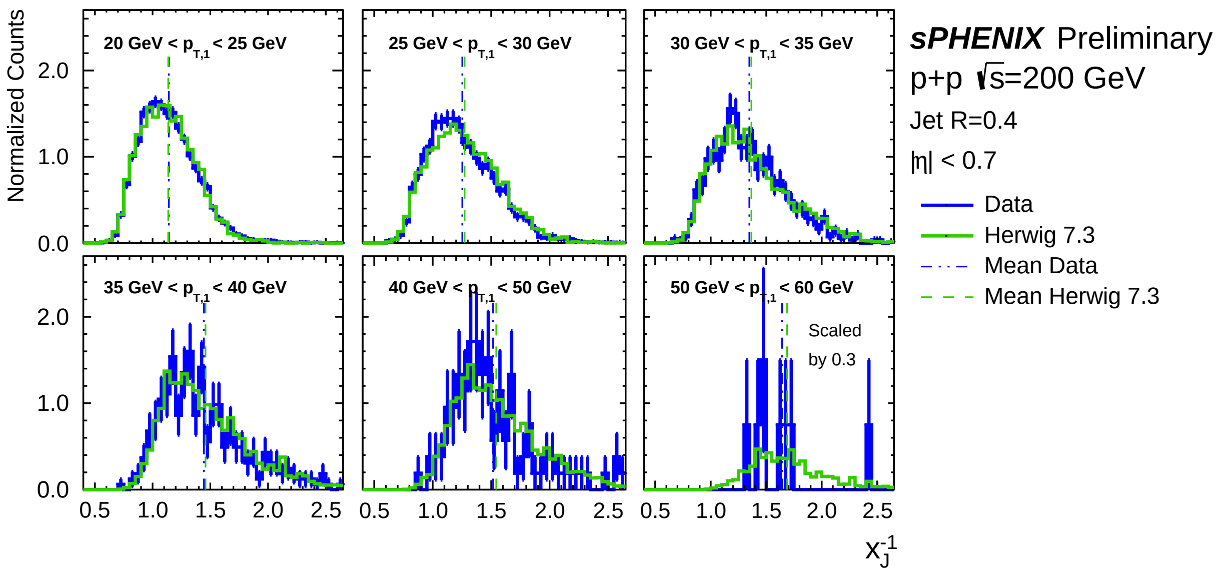

Figure 7: Distributions of multijet x_J^{-1} for the MBM analysis of $R = 0.4$ jets, shown separately for each $p_{T,1}$ interval in p+p data and reconstructed-level HERWIG-7.3 simulation. Statistical uncertainties on the data are shown as error bars, meanwhile the statistical uncertainties on the simulation are significantly smaller and not shown.

$p_{T,1}$ Range	$\langle x_J^{-1} \rangle$ (Data)	$\langle x_J^{-1} \rangle$ (HERWIG-7.3)	$\langle x_J{}^{-1} \rangle_{\text{Data}} / \langle x_J{}^{-1} \rangle_{\text{HERWIG-7.3}}$
20-25 GeV	1.141 ± 0.002	1.136 ± 0.003	1.004 ± 0.004
25-30 GeV	1.253 ± 0.005	1.272 ± 0.005	0.985 ± 0.007
30-35 GeV	1.348 ± 0.010	1.366 ± 0.006	0.986 ± 0.012
35-40 GeV	1.445 ± 0.020	1.458 ± 0.007	0.991 ± 0.022
40-50 GeV	1.516 ± 0.036	1.543 ± 0.006	0.982 ± 0.036
50-60 GeV	1.642 ± 0.112	1.688 ± 0.014	0.973 ± 0.113

Table 5: Summary of the multijet x_J^{-1} results in data and HERWIG-7.3 simulation for $R = 0.4$ jets, with each row showing a different $p_{T,1}$. Only statistical uncertainties are shown.

6 Global Data-to-MC JES correction

A global *in situ* Data-to-MC JES correction for the full jet p_{T} range is derived by combining the γ-jet and MBM results. Since the MBM results quantify the relative differences between jets at different p_{T} values, they alone do not provide a constraint on the absolute scale of the calibration. Rather, they are sensitive to the potential non-linearity of the Data-to-MC JES correction and cover the higher p_{T} region. The combination of the γ-jet and MBM results allow for a constraint on the absolute scale and the jet p_{T} dependence.

The global correction method assumes that there is a single JES calibration factor which is a polynomial function of jet p_{T} that, when applied, brings the $\langle x_{J\gamma} \rangle$ and $\langle x_J^{-1} \rangle$ values into agreement between data and simulation. The optimal parameters for the polynomial function are determined by applying each potential p_{T}-dependent correction and evaluating the resulting global χ^2 between data and simulation.

As mentioned earlier, correction functions linear in jet p_{T} were tested, which have the form $C(p_{\mathrm{T}}) = a + bp_{\mathrm{T}}$. Different parameter combinations were sampled in a fine grid over a broad parameter range, and the global minimum was determined, defined as before as the parameter set with the smallest total χ^2 between data and simulation, χ^2_{best}. The uncertainty in the parameters, and thus in the correction function, was determined by the parameter region where the $\chi^2 < \chi^2_{\mathrm{best}} + 2.30$, as we are now simultaneously fitting two parameters. Figure 8 shows the $\Delta\chi^2 = \chi^2 - \chi^2_{\mathrm{min}}$ distribution as a function of the two global fit parameters, a and b.

Figure 9 shows the agreement of the γ-jet and MBM results between data and simulation before and after the application of the Data-to-MC JES correction. As designed, the correction generally moves the data and simulation points into closer agreement.

Figure 10 shows the systematic uncertainties on the Data-to-MC JES correction as a function of jet p_{T}. The final correction function is taken to be the average of the best-fit results determined using Pythia-8 and Herwig-7.3 as the reference simulation samples, and the physics modeling uncertainty is taken as half the difference. At low jet-p_{T}, the uncertainty related to the purity of the γ-jet selection dominates, while at higher jet-p_{T}, many sources contribute equally.

Figure 11 shows the final global Data-to-MC JES correction for $R = 0.4$ jets as a function of jet p_{T}.

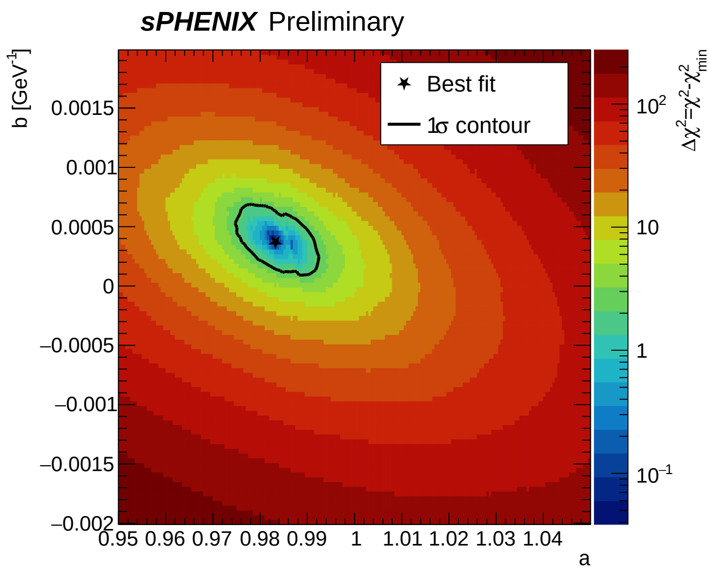

Figure 8: $\Delta\chi^2$ distribution as a function of the two global fit parameters, a and b. A black star shows the minimum χ^2 value. The black contour corresponds to the one standard deviation confidence region based on statistical uncertainties only.

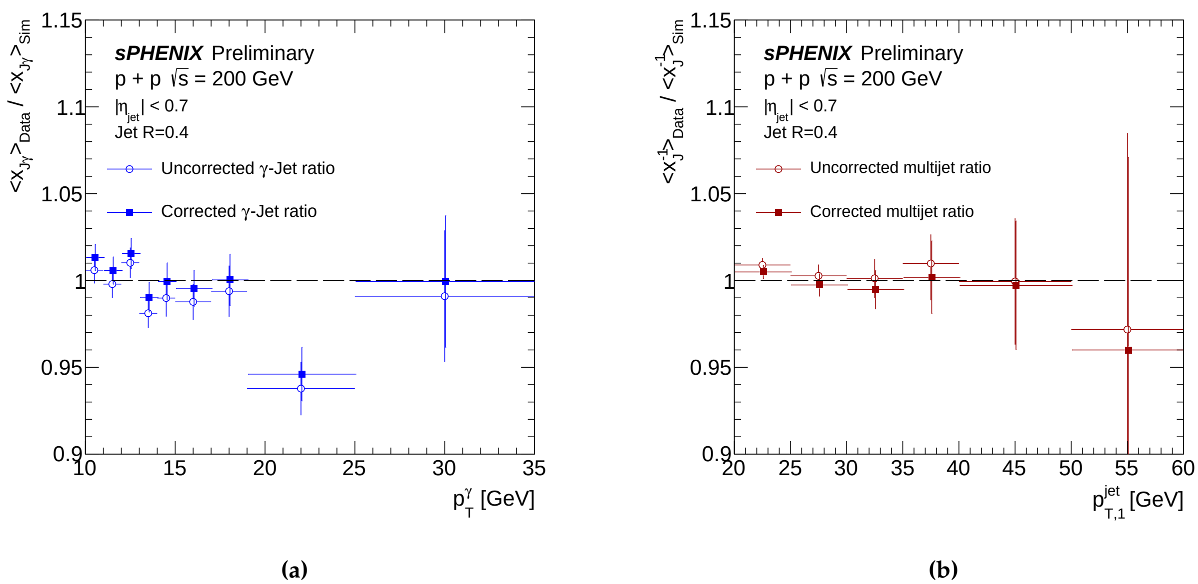

Figure 9: Comparison of data–simulation agreement (left) for the γ-jet analysis and (right) the MBM analysis, shown as the ratio of $\langle x_{J\gamma}\rangle$ and $\langle x_J^{-1}\rangle$, respectively, between data and simulation. The open and closed points correspond to the values before and after the application of the optimized Data-to-MC JES correction. A dashed line is drawn at 1 for a reference, and the points are slightly offset for visual clarity.

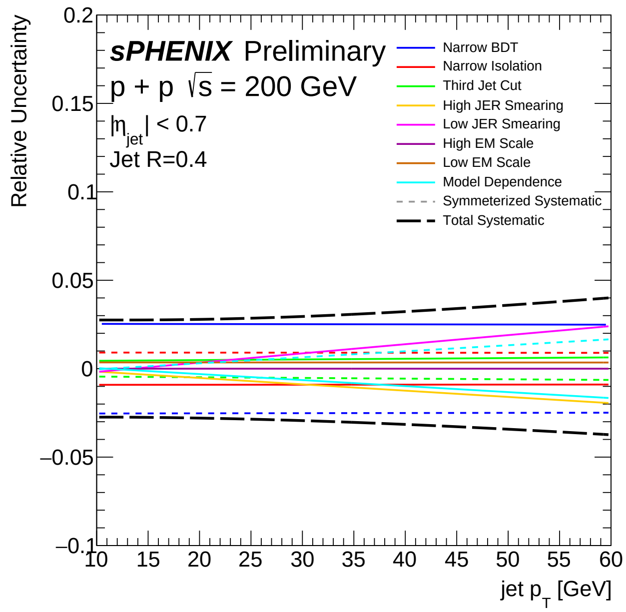

Figure 10: Summary of systematic uncertainties on the global JES correction function. The relative difference of the best-fit function to the nominal function is shown under the application of different systematic variations. All systematic uncertainty variations are symmetrized, except the separate high and low JER smearing and electromagnetic scaling, and then added in quadrature. The black dashed line shows the total systematic uncertainty.

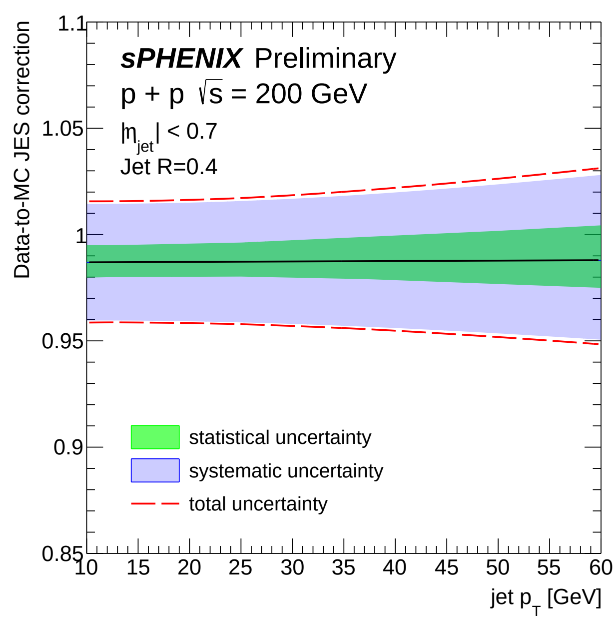

Figure 11: Global Data-to-MC JES correction as a function of calorimeter jet p_T, shown here for $R = 0.4$ jets. The black line is the central value. The green and blue shaded bands show the total statistical and systematic uncertainty, and the dashed red line shows the total uncertainty.

6.1 Application to other R values

The Data-to-MC JES correction above is derived for $R = 0.4$ jets. For larger-radius jets, multijet events with nearby jets are increasingly resolved as dijet events which leads to insufficient statistics for the MBM analysis. The absolute response for larger-R jets is still constrained by the γ-jet *in situ* analysis which, as shown in Table 3, does not reveal any significant R dependence. However, the Data-to-MC correction for jets with different R values has a stronger sensitivity to the physics model, as shown by the $\langle x_{J\gamma} \rangle$ values in Pythia-8 and Herwig-7.3 in Table 6.

Jet Radius	$\langle x_{J\gamma} \rangle_{\text{Pythia-8}} / \langle x_{J\gamma} \rangle_{\text{Herwig-7.3}}$	Systematic uncertainty
0.2	$0.9767^{+0.0192}_{-0.0083}$	0.0116
0.3	$0.9746^{+0.0167}_{-0.0060}$	0.0127
0.4	$0.9990^{+0.0094}_{-0.0131}$	0.0000
0.5	$1.0139^{+0.0111}_{-0.0087}$	0.0069
0.6	$1.0327^{+0.0085}_{-0.0125}$	0.0163
0.7	$1.0420^{+0.0082}_{-0.0092}$	0.0210
0.8	$1.0513^{+0.0112}_{-0.0174}$	0.0256

Table 6: Ratio of the $\langle x_{J\gamma} \rangle$ between Pythia-8 and Herwig-7.3, along with the statistical and systematic uncertainty.

Thus, to translate the global Data-to-MC JES correction to other R values, the correction for $R = 0.4$ jets can be applied but with an additional uncertainty contribution. This contribution is defined by taking half the physics model difference for the given R value in Table 6, and using that instead of the model systematic uncertainty for $R = 0.4$ jets. As an example, Figure 12 shows the resulting correction for $R = 0.8$ jets, where the uncertainties are modestly larger than for $R = 0.4$ jets.

7 Conclusions

The Data-to-MC JES correction provides a precise calibration of the absolute energy scale for calorimeter jets measured in sPHENIX. γ-jet events are used to set the absolute energy scale in a subset of the jet p_T range, where the JES correction can be extended to higher values of jet p_T using the multijet balance method. The Data-to-MC JES correction brings the jet response between data and simulation into agreement. The central value of the calibration is approximately 1–2% and is only weakly dependent on jet p_T and the jet radius parameter R. The uncertainty on the correction is 3–4%, varying with p_T and R. The Data-to-MC JES correction and its uncertainty are crucial to the precision sPHENIX jet physics program.

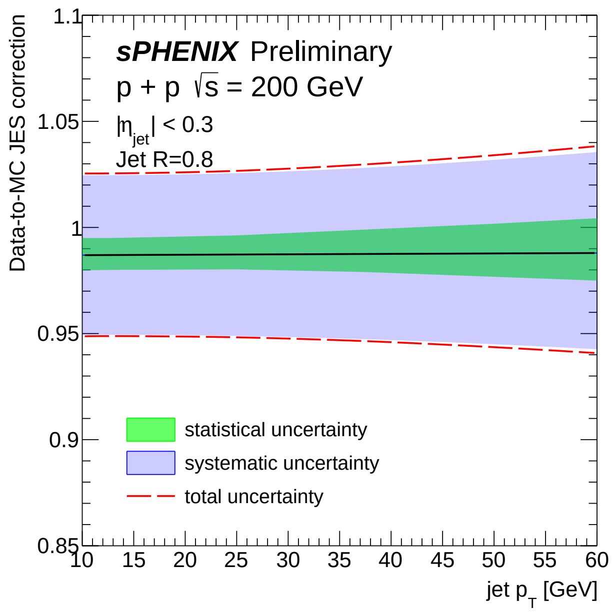

Figure 12: Global Data-to-MC JES correction as a function of calorimeter jet p_T shown for $R = 0.8$ jets. The black line is the central value. The green and blue shaded bands show the total statistical and systematic uncertainty, and the dashed red line shows the total uncertainty.

8 Appendix

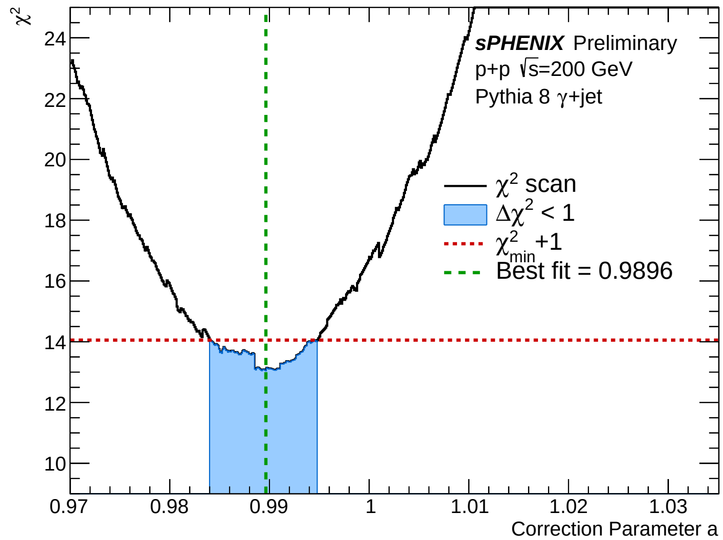

Figure 13: A visualization of the one-dimensional grid scan used for the γ-jet results in Section 4. The Data-to-MC JES correction using the γ-jet results alone assumes there is no p_{T} dependence, and the correction takes the form $C(p_{\mathrm{T}}) = a$, where the corrected jet in data is equal to $p_{\mathrm{T}}^{\mathrm{jet}}/C$. The statistical uncertainties on the correction are determined by grid values for which $\chi^2 < \chi^2_{\mathrm{min}} + 1$.

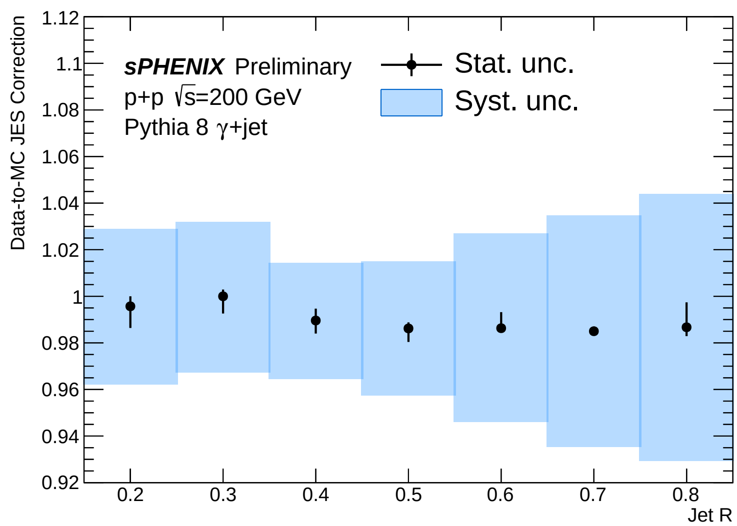

Figure 14: The Data-to-MC JES correction values from the γ-jet only constraint as shown in Table 1. The vertical error bars are the asymmetric statistical uncertainties, and the boxes are the total systematic uncertainties. Within uncertainties, there is no jet radius dependence to the Data-to-MC JES correction.

References

[1] Ron Belmont et al. Predictions for the sPHENIX physics program. *Nucl. Phys. A*, 1043:122821, 2024. arXiv:2305.15491, doi:10.1016/j.nuclphysa.2024.122821. 1

[2] B. Abbott et al. Determination of the absolute jet energy scale in the D0 calorimeters. *Nucl. Instrum. Meth. A*, 424:352–394, 1999. arXiv:hep-ex/9805009, doi:10.1016/S0168-9002(98)01368-0. 1

[3] A. Bhatti et al. Determination of the jet energy scale at the collider detector at Fermilab. *Nucl. Instrum. Meth. A*, 566:375–412, 2006. arXiv:hep-ex/0510047, doi:10.1016/j.nima.2006.05.269. 1

[4] Ariel Schwartzman. Jet energy calibration at the LHC. *Int. J. Mod. Phys. A*, 30(31):1546002, 2015. arXiv:1509.05459, doi:10.1142/S0217751X15460021. 1

[5] CMS Collaboration. Jet energy scale and resolution in the CMS experiment in pp collisions at 8 TeV. *JINST*, 12(02):P02014, 2017. arXiv:1607.03663, doi:10.1088/1748-0221/12/02/P02014. 1

[6] ATLAS Collaboration. A precise measurement of the jet energy scale derived from single-particle measurements and in situ techniques in proton-proton collisions at $\sqrt{s} = 13$ TeV with the ATLAS detector. *Eur. Phys. J. C*, 85(9):927, 2025. arXiv:2407.15627, doi:10.1140/epjc/s10052-025-14409-1. 1, 5

[7] sPHENIX Collaboration. Measurement of the transverse energy density in Au+Au collisions at $\sqrt{s_{\mathrm{NN}}}$= 200 GeV with the sPHENIX detector. *Phys. Rev. C*, 112(2):024908, 2025. arXiv:2504.02242, doi:10.1103/h8d5-swg6. 1

[8] Matteo Cacciari, Gavin P. Salam, and Gregory Soyez. The anti-k_t jet clustering algorithm. *JHEP*, 04:063, 2008. arXiv:0802.1189, doi:10.1088/1126-6708/2008/04/063. 1, 3

[9] sPHENIX Collaboration. sPHENIX Technical Design Report, PD-2/3 Release, 2019. URL: https://indico.bnl.gov/event/7081/attachments/25527/38284/sphenixtdr20190513.pdf. 2

[10] sPHENIX Collaboration. Measurement of isolated prompt photons in p+p collisions at $\sqrt{s}$ = 200 GeV with the sPHENIX detector. URL: https://www.sphenix.bnl.gov/PublicResults/sPH-CONF-JET-2025-02. 2, 3

[11] Christian Bierlich et al. A comprehensive guide to the physics and usage of PYTHIA 8.3. *SciPost Phys. Codeb.*, 2022:8, 2022. arXiv:2203.11601, doi:10.21468/SciPostPhysCodeb.8. 2

[12] Manny Rosales Aguilar, Zilong Chang, Raghav Kunnawalkam Elayavalli, Renee Fatemi, Yang He, Yuanjing Ji, Dmitry Kalinkin, Matthew Kelsey, Isaac Mooney, and Veronica Verkest. Pythia8 underlying event tune for RHIC energies. *Phys. Rev. D*, 105(1):016011, 2022. arXiv:2110.09447, doi:10.1103/PhysRevD.105.016011. 2

[13] Johannes Bellm et al. Herwig 7.0/Herwig++ 3.0 release note. *Eur. Phys. J. C*, 76(4):196, 2016. arXiv:1512.01178, doi:10.1140/epjc/s10052-016-4018-8. 2

[14] Gavin Bewick et al. Herwig 7.3 release note. *Eur. Phys. J. C*, 84(10):1053, 2024. arXiv:2312.05175, doi:10.1140/epjc/s10052-024-13211-9. 2

[15] Umar Sohail Qureshi, Luke Mozarsky, Helen Caines, Raghav Kunnawalkam Elayavalli, and Isaac Mooney. New herwig7 underlying event tune: From RHIC to LHC energies. *Phys. Rev. D*, 112(11):116019, 2025. `arXiv:2411.16897`, `doi:10.1103/cnck-wtbh`. 2

[16] S. Agostinelli et al. GEANT4 - A Simulation Toolkit. *Nucl. Instrum. Meth. A*, 506:250–303, 2003. `doi:10.1016/S0168-9002(03)01368-8`. 2

[17] sPHENIX Collaboration. Measurement of dijet transverse momentum imbalance and azimuthal acoplanarity in p+p collisions at $\sqrt{s} = 200$ GeV with the sPHENIX detector. 2026. `arXiv:2606.17184`. 3, 4.1

[18] Matteo Cacciari, Gavin P. Salam, and Gregory Soyez. FastJet User Manual. *Eur. Phys. J. C*, 72:1896, 2012. `arXiv:1111.6097`, `doi:10.1140/epjc/s10052-012-1896-2`. 3

[19] G. David, E. Kistenev, S. White, C. Woody, A. Bazilevsky, S. Belikov, V. Kochetkov, V. Onuchin, and A. Usachev. Pattern recognition in the PHENIX PbSc electromagnetic calorimeter. *IEEE Trans. Nucl. Sci.*, 47:1982–1986, 2000. `doi:10.1109/23.903833`. 3